Advances and Applications in Fluid Mechanics
Volume 1, Issue 1, 2007, Pages 1-35
This paper is available online at http://www.pphmj.com

USING ISOTROPIC SYNTHETIC FLUCTUATIONS AS INLET BOUNDARY CONDITIONS FOR UNSTEADY SIMULATIONS

L. DAVIDSON

Division of Fluid Dynamics
Department of Applied Mechanics
Chalmers University of Technology
SE-412 96 Göteborg, Sweden

Abstract

The paper proposes a method to prescribe synthesized turbulent inlet boundary conditions. When making LES, DES or hybrid LES-RANS a precursor channel DNS is often used. The disadvantage of this method is that it is difficult to re-scale the DNS fluctuations to higher Reynolds numbers. In the present work synthesized isotropic turbulent fluctuations are generated at the inlet plane with a prescribed turbulent length scale and energy spectrum. A large number of independent realizations are generated. A correlation in time between these realization is introduced via an asymmetric, non-truncated time filter. In this way the turbulent time scale of the synthesized isotropic turbulent fluctuations is prescribed.

The method is first validated for DNS at Re_τ = 500. It is then employed in hybrid LES-RANS of channel flow at Re_τ = 2000 on a coarse mesh. The sensitivity to different prescribed inlet length scales, time scales and amplitudes of the fluctuations is investigated.

2000 Mathematics Subject Classification: 76F65.

Keywords and phrases: hybrid LES-RANS, forcing fluctuations, trigger resolved turbulence, embedded LES.

Communicated by Shahrdad G. Sajjadi

Received August 22, 2006

The inlet boundary conditions have much in common with forcing fluctuations in the interface region in hybrid LES-RANS. In both cases the object is to *trigger* the equations to resolve turbulence. The method of generating inlet boundary conditions is also relevant in embedded LES, where LES is used on a mesh embedded in a global steady or unsteady RANS computation.

1. Introduction

Inlet boundary conditions are important when making Large Eddy Simulation. In high Reynolds number flow the grid is mostly too coarse to resolve any large portion of the turbulent spectrum. This is especially so near the inlet, where few cells are commonly located in order to reduce the number of cells; the majority of the cells are allocated to resolve boundary layers, wakes and recirculating regions. The grids are even coarser in hybrid LES-RANS and DES and the grid spacing may be larger than the turbulent integral length scale. The object of the inlet boundary conditions is then not to supply turbulence with the *correct* time and length scales, but to supply scales relevant to the grid. In other words, the inlet turbulence should have integral length and time scales related to the grid size, Δx, Δy, Δz, and the computational time step Δt, i.e., scales that the Navier-Stokes equations on the given grid understand. The object of the inlet boundary conditions is to *trigger* the equations to resolve turbulence.

In hybrid LES-RANS, URANS (Unsteady Reynolds-Averaged Navier-Stokes) is used near the walls and LES is used at a certain distance away from the wall [9, 13, 24-26, 28], see Fig. 1. The location at which the switch is made from URANS to LES is called the *interface*. Instead of resolving the near-wall turbulent structures, they are modelled with the RANS turbulence model. A drawback of hybrid LES-RANS is that, at the interface where the turbulence model equations switch from URANS to LES, the LES gets poor interface conditions from the URANS. The unsteadiness that is convected from the URANS region to the LES region contains no proper turbulent scales. To supply the LES region with proper turbulent scales it was suggested that turbulent fluctuations (forcing) should be added as momentum sources in the URANS region, in the interface region or in the interface [2, 7, 10, 11, 18, 22, 24] of the

URANS region and the LES region. This forcing at the interface is similar to prescribing fluctuating velocity fluctuations (forcing) at the inlet. The object is in both cases the same: to efficiently as possible force the momentum equations into turbulent mode.

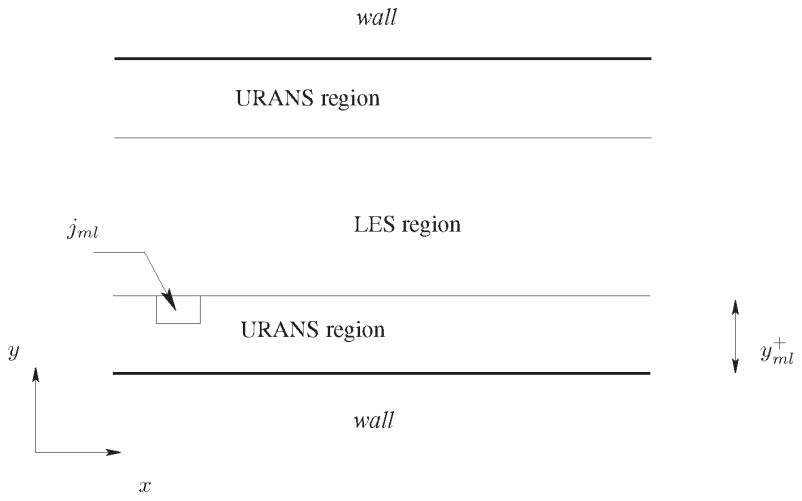

Figure 1. The LES and URANS regions. The interface is located at $y^+ = y^+_{ml}$ and the number of cells in the URANS region in the wall-normal direction is j_{ml}.

The currently most popular method of generating turbulent inlet boundary conditions is to make a precursor DNS of channel flow or boundary layer flow. This is an accurate method provided that the Reynolds number of the DNS is relevant. If the Reynolds number of the DNS is too low, then it is not clear how to re-scale the DNS fluctuations. While it is easy to re-scale the amplitude of the fluctuations, it is difficult to re-scale the turbulent length and time scales.

Isotropic synthesized fluctuations based on the method of Kraichnan [17] have often been used to generate turbulent fluctuations, see e.g. [1, 3, 15, 21]. In this method an energy spectrum is prescribed that yields the amplitude of the fluctuations as a function of wave number. Non-isotropic fluctuations were generated in [2, 5, 6, 19, 20, 23] and the fluctuations were scaled so that the time-averaged synthesized fluctuations match a prescribed Reynolds stress tensor. A disadvantage of this kind of scaling

is that the prescribed spectrum, and hence the two-point correlation, are modified if the Reynolds stress tensor is non-homogeneous.

To achieve correlation in time, Fourier series were applied in time in the same way as in space in most of the works cited above. In [21] a method was also investigated where a three-dimensional box with generated fluctuations was convected across the inlet plane; in this way fluctuation correlations in the streamwise directions were transformed into correlations in time. In the work by Billson et al. correlation in time is defined by an asymmetric infinite time filter. The method offers a convenient way to prescribe turbulent length and time scales independently. This method is adopted in the present work.

A method based partly on synthesized fluctuations was recently presented and it is called the *vortex method* [14]. It is based on a superposition of coherent eddies where each eddy is described by a shape function that is localized in space. The eddies are generated randomly in the inflow plane and then convected through it. The method is able to reproduce first and second-order statistics as well as two-point correlations.

Channel flow is a common test case for testing hybrid LES-RANS. Since this flow is entirely dependent on the near-wall turbulence, it is a challenging test case. It is also a useful test case for evaluating inlet boundary conditions. In the present study we use hybrid LES-RANS, and the computational grid is – purposely – very coarse. A mean velocity profile is prescribed, that is taken from the law of the wall. Turbulent instantaneous fluctuations are superimposed on the mean profile. These fluctuations are taken from synthesized, isotropic turbulence prescribing the turbulent integral length scale. A large number of independent synthesized velocity fields are created that are independent of each other, which means that the time correlation is zero. The turbulent time scale is prescribed using a suitable linear combination of the running time average (from zero to time t) of the inlet fluctuations and the fluctuating field at time t. The influence of different integral lengths, time scales and amplitudes of the turbulent inlet boundary conditions is investigated.

The paper is organized as follows. The equations and the standard

hybrid LES-RANS model are first presented. The method for generating synthetic fluctuations is then described and a brief presentation is given of the numerical method and the hybrid LES-RANS model. In the results section, we start with DNS simulation continue with hybrid LES-RANS, and end with some results of using hybrid LES-RANS with forcing at the interface. The paper ends with the conclusions.

2. Equations

The Navier-Stokes equations with an added turbulent/SGS viscosity read

$$\frac{\partial \overline{u}_i}{\partial t} + \frac{\partial}{\partial x_j}(\overline{u}_i \overline{u}_j) = \beta \delta_{1i} - \frac{1}{\rho}\frac{\partial \overline{p}}{\partial x_i} + \frac{\partial}{\partial x_j}\left[(\nu + \nu_T)\frac{\partial \overline{u}_i}{\partial x_j}\right], \tag{1}$$

$$\frac{\partial \overline{u}_i}{\partial x_i} = 0, \tag{2}$$

where $\nu_T = \nu_t$ (ν_t denotes the turbulent RANS viscosity) for $y \le y_{ml}$ (see Fig. 1), and for $y > y_{ml}$ we use $\nu_T = \nu_{sgs}$. The switch between URANS and LES is achieved in the same way at the upper matching plane (at $2\delta - y_{ml}$). Coefficient $\beta = 1$ is used for channel flow simulations with periodic streamwise boundary conditions; when inlet-outlet boundary conditions are used, $\beta = 0$. The density is set to one in all simulations.

3. Synthesized Turbulence

A turbulent velocity field can be simulated using random Fourier modes. This was proposed in [17] and later developed further in [1, 3, 15, 21]. The velocity field is given by N random Fourier modes as

$$u_i'(x_j) = 2\sum_{n=1}^{N} \hat{u}^n \cos(\kappa_j^n x_j + \psi^n)\sigma_i^n, \tag{3}$$

where $\hat{u}^n$, ψ^n and σ_i^n are the amplitude, phase and direction of Fourier mode n, respectively. The notation used here follows that in [4, 6, 10] and more information is given in these papers. The synthesized turbulence at one time step is generated as follows.

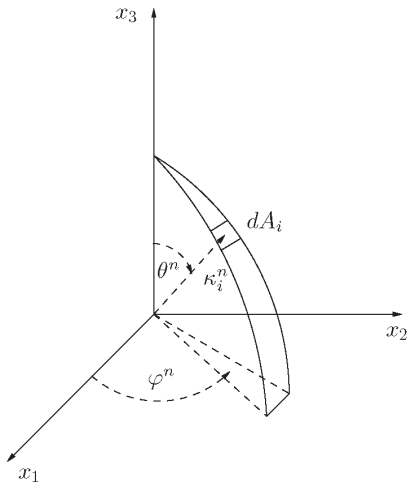

Figure 2. The probability of a randomly selected direction of a wave in wave-space is the same for all dA_i on the shell of a sphere.

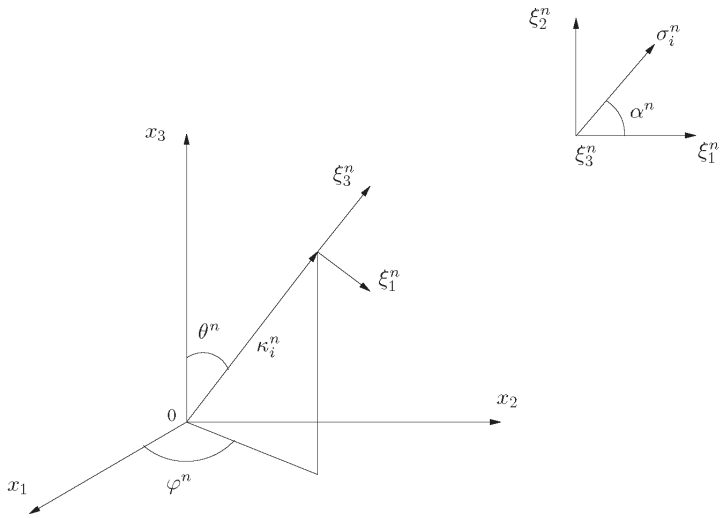

Figure 3. The wave-number vector, κ_i^n, and the velocity unit vector, σ_i^n, are orthogonal (in physical space) for each wave number n. The unit vector, σ_i^n, is defined such that $\sigma_i^n \kappa_i^n = 0$ (superscript n denotes Fourier mode n). Furthermore, σ_3^n is parallel to κ_i^n (i.e., $\sigma_3^n = \xi_3^n$). The direction of σ_i^n in the $\xi_1^n - \xi_2^n$ plane is randomly chosen through α^n.

1. For each mode n, create random angles φ^n, α^n and θ^n (see Figs. 2 and 3) and random phase ψ^n. The probability distributions are given in Table 1.

Table 1. Probability distributions of the random variables

$p(\varphi^n) = 1/(2\pi)$	$0 \le \varphi^n \le 2\pi$
$p(\psi^n) = 1/(2\pi)$	$0 \le \psi^n \le 2\pi$
$p(\theta^n) = 1/2 \sin(\theta)$	$0 \le \theta^n \le \pi$
$p(\alpha^n) = 1/(2\pi)$	$0 \le \alpha^n \le 2\pi$

2. Define the highest wave number based on mesh resolution $\kappa_{\max} = 2\pi/(2\Delta)$, where Δ is the grid spacing. The fluctuations are generated on a grid with equidistant spacing, $\Delta\eta = y_{\max}/N_j$, $\Delta z = z_{\max}/N_k$, where η denotes the wall-normal direction and N_j and N_k denote the number of cells in the y and z directions, respectively. The fluctuations are set to zero at the wall and are then interpolated to the inlet plane of the CFD grid (the $y - z$ plane).

3. Define the smallest wave number from $\kappa_1 = \kappa_e/p$, where $\kappa_e = \alpha 9\pi/(55L_t)$, $\alpha = 1.453$. Factor p should be larger than one to make the largest scales larger than those corresponding to κ_e. In the present work $p = 2$.

4. Divide the wavenumber space, $\kappa_{\max} - \kappa_1$, into N modes, equally large, of size $\Delta\kappa$.

5. Compute the randomized components of κ_j^n according to Fig. 2.

6. Continuity requires that the unit vector, σ_i^n, and κ_j^n are orthogonal. σ_3^n is arbitrarily chosen to be parallel with κ_i^n (see Fig. 3), and α^n and the requirement of orthogonality give the remaining two components.

7. A modified von Kármán spectrum is chosen, see Eq. 4 and Fig. 4. The amplitude $\hat{u}^n$ of each mode in Eq. 3 is then obtained from $\hat{u}^n = (E(|\kappa_j^n|)\Delta\kappa)^{1/2}$.

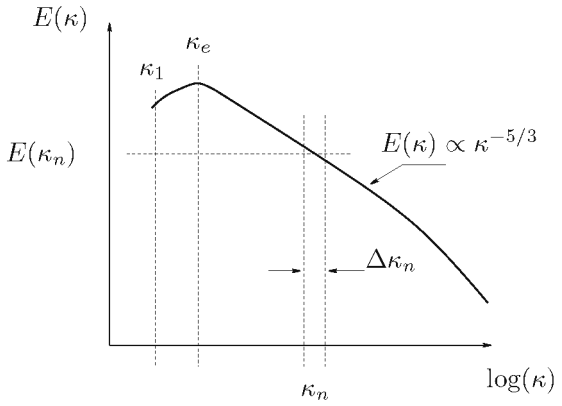

Figure 4. Modified von Kármán spectrum.

8. Having $\hat{u}^n$, κ_j^n, σ_i^n and ψ^n, allows the expression in Eq. 3 to be computed.

$$E(\kappa) = \alpha \frac{u_{rms}^2}{\kappa_e} \frac{(\kappa/\kappa_e)^4}{[1 + (\kappa/\kappa_e)^2]^{17/6}} e^{[-2(\kappa/\kappa_\eta)^2]}$$

$$\kappa = (\kappa_i \kappa_i)^{1/2}, \quad \kappa_\eta = \varepsilon^{1/4} \nu^{-3/4}. \tag{4}$$

In this way inlet fluctuating velocity fields (u', v', w') are created at the inlet $y - z$ plane.

A fluctuating velocity field is generated each time step as described above. They are independent of each other, however, and their time correlation will thus be zero. This is unphysical. To create correlation in time, new fluctuating velocity fields, $\mathcal{U}'$, $\mathcal{V}'$, $\mathcal{W}'$, are computed based on an asymmetric time filter, as in [4, 6]

$$(\mathcal{U}')^m = a(\mathcal{U}')^{m-1} + b(u')^m$$

$$(\mathcal{V}')^m = a(\mathcal{V}')^{m-1} + b(v')^m$$

$$(\mathcal{W}')^m = a(\mathcal{W}')^{m-1} + b(w')^m, \tag{5}$$

where m denotes the time step number and $a = \exp(-\Delta t/\mathcal{T})$. This asymmetric time filter resembles the spacial digital filter presented in [16]. The second coefficient is taken as $b = (1 - a^2)^{0.5}$ which ensures that $\langle \mathcal{U}_i'^2 \rangle = \langle u_i'^2 \rangle$ ($\langle \cdot \rangle$ denotes averaging). The time correlation of $\mathcal{U}_i'$ will be equal to $\exp(-\Delta t/\mathcal{T})$, and thus Eq. 5 is a convenient way to prescribe the turbulent time scale of the fluctuations. The inlet boundary conditions are prescribed as

$$\begin{aligned} \overline{u}(0,\ y,\ z,\ t) &= U_{in}(y) + u'_{in}(y,\ z,\ t) \\ \overline{v}(0,\ y,\ z,\ t) &= V_{in}(y) + v'_{in}(y,\ z,\ t) \\ \overline{w}(0,\ y,\ z,\ t) &= W_{in}(y) + w'_{in}(y,\ z,\ t), \end{aligned} \tag{6}$$

where $u'_{in} = (\mathcal{U}')^m$, $v'_{in} = (\mathcal{V}')^m$ and $w'_{in} = (\mathcal{W}')^m$ (see Eq. 5). For the hybrid LES-RANS simulations at $Re_\tau = 2000$, the mean velocities are set as $V_{in} = W_{in} = 0$ and [27]

$$U_{in}^+ = \begin{cases} y^+ & y^+ \le 5 \\ -3.05 + 5\ln(y^+) & 5 < y^+ < 30 \\ \dfrac{1}{\kappa}\ln(y^+) + B & y^+ \ge 30, \end{cases} \tag{7}$$

where $\kappa = 0.4$ and $B = 5.2$. For the DNS at $Re_\tau = 500$, the mean streamwise velocity, U_{in}, is taken from a DNS of fully developed flow (streamwise periodic boundary conditions).

4. The Numerical Method

An incompressible, finite volume code is used [9]. For space discretization, central differencing is used for all terms. The Crank-Nicholson scheme is used for time discretization of all equations. The numerical procedure is based on an implicit, fractional step technique with a multigrid pressure Poisson solver [12] and a non-staggered grid arrangement.

5. Hybrid LES–RANS

A one-equation model is employed in both the inner URANS region and outer LES region and reads

$$\frac{\partial k_T}{\partial t} + \frac{\partial}{\partial x_j}(\overline{u}_j k_T) = \frac{\partial}{\partial x_j}\left[(\nu + \nu_T)\frac{\partial k_T}{\partial x_j}\right] + P_{k_T} - C_\varepsilon \frac{k_T^{3/2}}{\ell}$$

$$P_{k_T} = -\tau_{ij}\overline{s}_{ij}, \quad \tau_{ij} = -2\nu_T \overline{s}_{ij}. \tag{8}$$

In the inner region $(y \le y_{ml})$ k_T corresponds to the RANS turbulent kinetic energy k; in the outer region $(y > y_{ml})$ it corresponds to the subgrid-scale kinetic turbulent energy k_{sgs}. No special treatment is used in the equations at the matching plane except that the form of the turbulent viscosity and the turbulent length scale are different in the two regions, see Table 2. $k_T = 0$ at the walls and $\partial k_T/\partial x = 0$ at the inlet.

Table 2. Turbulent viscosities and turbulent length scales in the URANS and LES regions. n and δV denote the distance to the nearest wall and the computational cell volume, respectively

	URANS region	LES region
l	$2.5n[1 - \exp(-0.2k^{1/2}\, n/\nu)]$	$\ell = \Delta = (\delta V)^{1/3}$
ν_T	$2.5k^{1/2}n[1 - \exp(-0.014k^{1/2}\, n/\nu)]$	$0.07k_{sgs}^{1/2}\ell$
C_ε	1.0	1.05

6. Results

6.1. Direct Numerical Simulations

The mesh has $256 \times 80 \times 64$ in the streamwise (x), wall-normal (y) and spanwise (z) directions, respectively. The turbulent viscosity, ν_T, in Eq. 1 is set to zero. The size of the computational domain is $x_{\max} = 8\pi$, $y_{\max} = 2\delta = 2$ (geometric stretching of 12%) and $z_{\max} = 0.5\pi$. This gives

a Δx^+ and Δz^+ of approximately 50 and 12, respectively, and $y^+ \simeq 0.3$ for the near-wall node. The time step was set to $\Delta t u_\tau/\delta = 1.23 \cdot 10^{-3}$ which gives a maximal CFL of approximately one. The Reynolds number is $Re_\tau = u_\tau \delta/\nu = 500$. Neumann boundary outlet boundary conditions were initially used but they were found to disturb the solution upstream of the outlet. Instead convective outlet boundary conditions were prescribed as

$$\frac{\partial u_i}{\partial t} + U_0 \frac{\partial u_i}{\partial x} = 0, \tag{9}$$

where $U_0(y, t) = \int_0^{z_{\max}} \int_0^t u(x_{\max}, y, z, t')dzdt'$. Fluctuating inlet velocity boundary conditions with different time scales, length scales and amplitudes are investigated, see Table 3.

Table 3. Presentation of test cases for the DNS simulations. The baseline turbulent length and time scales are set to $\mathcal{L}_1 = 0.11 = L_t$ and $\mathcal{T}_1 = \mathcal{T} = 0.22$ (see Section 3), respectively. The baseline amplitude of the inlet fluctuations is $u_{in,rms} = v_{in,rms} = w_{in,rms} = 1.5$. Constants a and b from Eq. 5 are also given.

$\mathcal{L}$	$\mathcal{T}$	$u_{in,rms}$	a	b
$\mathcal{L}_1$	$\mathcal{T}_1$	1.5	0.995	0.104
$\mathcal{L}_1$	$\mathcal{T}_1/4$	1.5	0.978	0.207
$\mathcal{L}_1$	$\mathcal{T}_1/12$	1.5	0.936	0.351
$\mathcal{L}_1$	$\mathcal{T}_1/12$	0.75	0.936	0.351
$\mathcal{L}_1$	$\mathcal{T}_1/12$	2.25	0.936	0.351
$\mathcal{L}_1/2$	$\mathcal{T}_1/12$	1.5	0.936	0.351
$\mathcal{L}_1/4$	$\mathcal{T}_1/12$	1.5	0.936	0.351
$1.5\mathcal{L}_1$	$\mathcal{T}_1/12$	1.5	0.936	0.351

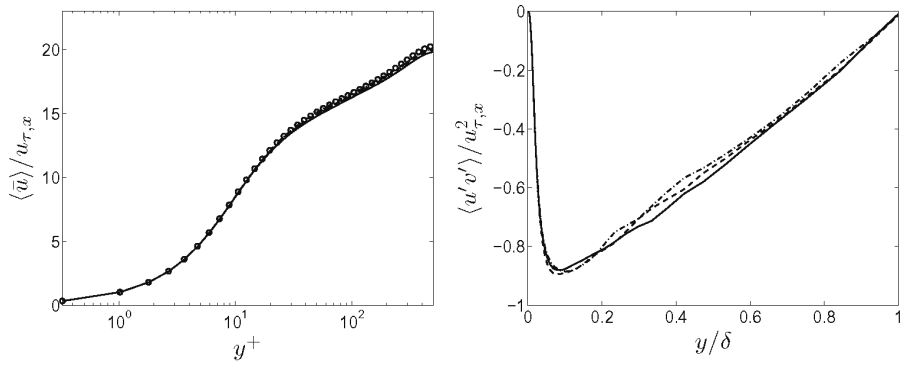

(a) $\langle \bar{u} \rangle$ profiles. (b) Resolved shear stresses.

Figure 5. Mean velocities and resolved shear stresses. DNS inlet fluctuating velocities. — : $x/\delta = 1$; --- : $x/\delta = 10$; -·- : $x/\delta = 24$.

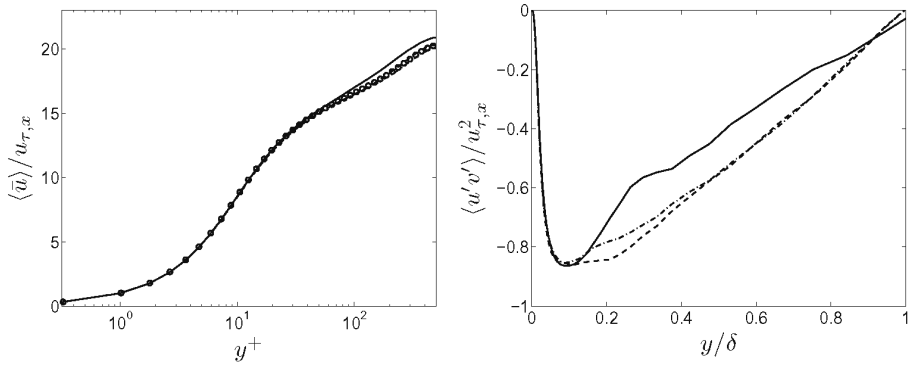

(a) $\langle \bar{u} \rangle$ profiles. (b) Resolved shear stresses.

Figure 6. Mean velocities and resolved shear stresses. Synthesized isotropic inlet fluctuating velocities. $u_{in,rms} = v_{in,rms} = w_{in,rms} = 1.5$. Inlet time scale $\mathcal{T}_1/12$ and inlet length scale $\mathcal{L}_1$. — : $x/\delta = 1$; --- : $x/\delta = 10$; -·- : $x/\delta = 24$.

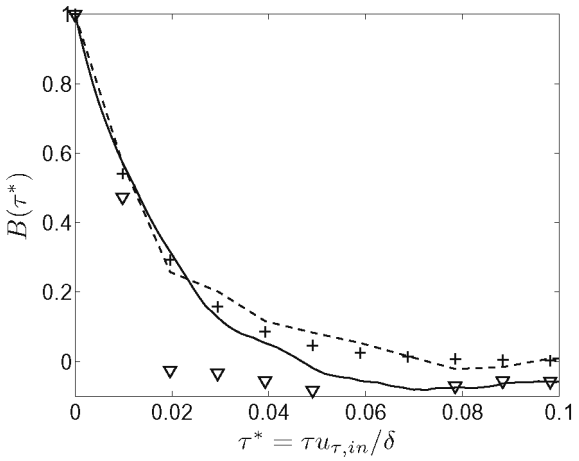

Figure 7. Autocorrelation $B(\tau) = 1/(Tu_{in,rms}^2)\int_0^T u'_{in}(t)u'_{in}(t-\tau)dt$. — : synthetic fluctuations with $\mathcal{T}_1/12$; --- : DNS fluctuations at $y^+ \simeq 130$; ∇ : DNS fluctuations at $y^+ \simeq 380$; + : $\exp(-12\tau)/\mathcal{T}_1$.

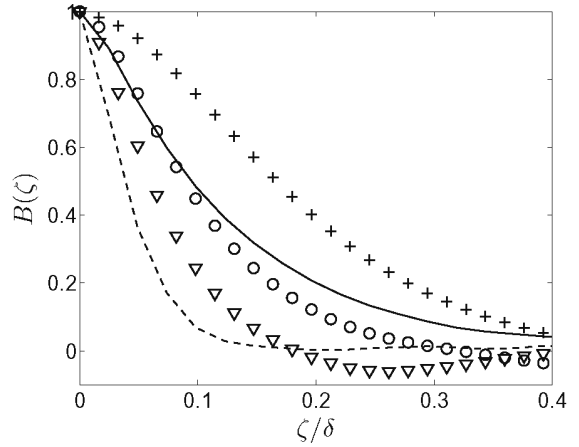

Figure 8. Two-point correlation $B(\zeta) = 1/(z_{\max}w_{in,rms}^2)\int_0^{z_{\max}} w'_{in}(z)\, w'_{in}(z-\zeta)dz$. $x = 0$. — : synthetic fluctuations with $\mathcal{L}_1$; --- : synthetic fluctuations with $\mathcal{L}_1/4$; ∇ : fully developed channel DNS at $y^+ \simeq 20$; o : fully developed channel DNS at $y^+ \simeq 60$; + : fully developed channel DNS at $y^+ \simeq 500$.

The velocity profile and the resolved shear stresses are shown in Fig. 5 (DNS inlet fluctuations) and Fig. 6 (synthesized fluctuations using inlet time scale $\mathcal{T}_1/12$ and inlet length scale $\mathcal{L}_1$). The profiles are shown for $x = \delta$, $x = 10\delta$ and $x = 24\delta$. The velocity profiles agree very well with DNS data for both cases. The resolved shear stresses are slightly better with DNS fluctuations than with synthesized fluctuations. Still, the synthetic isotropic fluctuations do a remarkable job considering that the prescribed inlet shear stress is zero; they manage to trigger the equations to yield a reasonable shear stress profile even at $x = \delta$. The length and time scales used in Fig. 6 give autocorrelation and two-point correlations that agree well with fully developed DNS at $y^+ = 130$ and 60, respectively, see Figs. 7 and 8. The two-point correlations and the autocorrelations of the isotropic fluctuations are constant with respect to y, since the y and z coordinates are treated as homogeneous directions when the synthetic fluctuations are generated. The true autocorrelations and two-point correlations decrease as the wall is approached. The two-point correlations evaluated from DNS at different y locations are included in Fig. 8. This illustrates the fact that the prescribed turbulent time and length scales of the synthetic homogeneous isotropic fluctuations agree with the physical correlation only in some average sense.

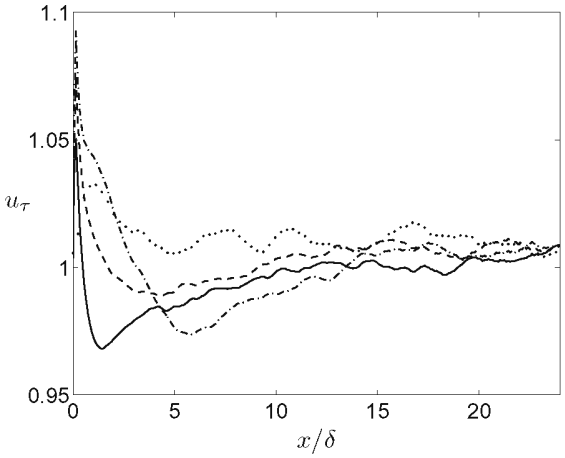

Figure 9. Friction velocity. Investigation of sensitivity to different inlet time scales. $u_{in,rms} = v_{in,rms} = w_{in,rms} = 1.5$. Inlet length scale $\mathcal{L}_1$. — : $\mathcal{T}/12$; --- : $\mathcal{T}/4$; -·- : $\mathcal{T}$; ··· : DNS.

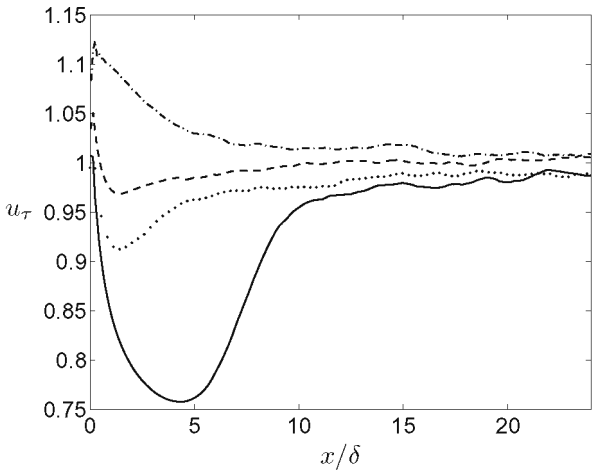

Figure 10. Friction velocity. Investigation of sensitivity to different amplitudes of inlet synthetic isotropic fluctuations. Inlet time scale $\mathcal{T}_1/12$ and inlet length scale $\mathcal{L}_1$. — : $u_{in,rms} = v_{in,rms} = w_{in,rms} = 0.75$; --- : $u_{in,rms} = v_{in,rms} = w_{in,rms} = 1.5$; -·- : $u_{in,rms} = v_{in,rms} = w_{in,rms} = 2.25$; ⋯ : synthetic fluctuations re-scaled to fit RMS profiles of DNS.

The influence of different time scales is shown in Fig. 9. DNS inlet fluctuations and synthetic inlet fluctuations with $\mathcal{T}_1/4$ and $\mathcal{T}_1/12$ give a friction velocity within 1% of the target value, $u_\tau = 1$, at approximately $x = 5\delta$. The larger the time scale, the greater the over-prediction of the friction velocity near the inlet.

The amplitude of the synthetic fluctuations used in the prediction presented so far was set to 1.5. How does a change in amplitude affect the results? Different amplitudes have been used in Fig. 10. It can be seen that the sensitivity to the inlet amplitude is much stronger than the sensitivity to the inlet time scale. When a small amplitude of the fluctuations is used $(u_{in,rms} = 0.75)$ it is just about that the inlet fluctuations manage to trigger the equations to resolve turbulence. It takes 10δ until the friction velocity is within 4% of its target value. A large amplitude gives an overshoot in the friction velocity near the inlet but, contrary to when a small amplitude is employed, no undershoot in the friction velocity appears.

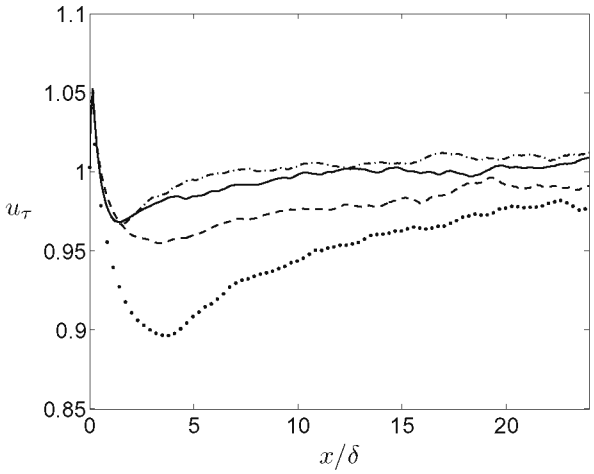

Figure 11. Friction velocity. Investigation of sensitivity to different inlet turbulent length scales. Inlet time scale $\mathcal{T}_1/12$. — : length scale $\mathcal{L}_1$; --- : length scale $\mathcal{L}_1/2$; -·- : length scale $1.5\mathcal{L}_1$; ··· : length scale $\mathcal{L}_1/4$.

Figure 11 investigates the influence of different turbulent length scales of the inlet fluctuations. As can be seen, the effect of changing the length scale is larger than that of changing the time scale. The larger the length scale of the inlet fluctuations, the more efficient they are in triggering the equations. The simulations diverged when larger length scale than $1.5\mathcal{L}_1$ was tested.

Resolved shear stresses and wall-normal RMS fluctuations at a station close to the inlet, are shown in Figs. 12 (different time scales) and 13 (different amplitudes). Here it is confirmed what was seen in the friction velocities: large time scales and large amplitudes are efficient in triggering resolved turbulence, and the equations are more sensitive to changes in amplitude than to changes in time scale. Recall that at the inlet, $u_{in,rms} = v_{in,rms} = w_{in,rms} = const$ across the channel except for $y/\delta < 1/N_j = 1/80$ (lower wall) and $y/\delta > 2 - 1/N_j$ (upper wall), see Section 3, where the instantaneous fluctuations are obtained by linear interpolation (zero value of the fluctuations at the wall).

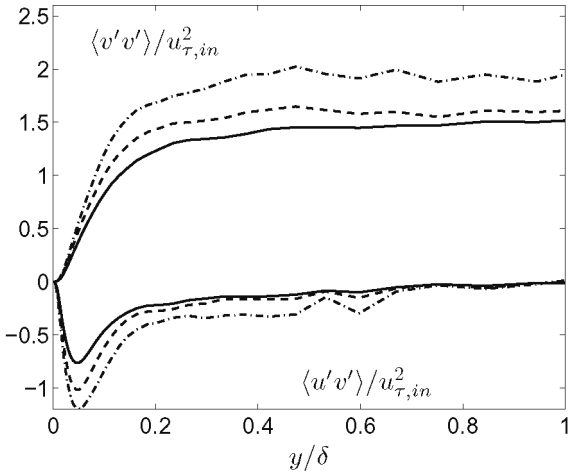

Figure 12. Shear stresses and wall-normal stresses. $x = 0.35\delta$. Investigation of sensitivity to different inlet time scales. $u_{in,rms} = v_{in,rms} = w_{in,rms} = 1.5$. — : $\mathcal{T}/12$; --- : $\mathcal{T}/4$; ··· : $\mathcal{T}$.

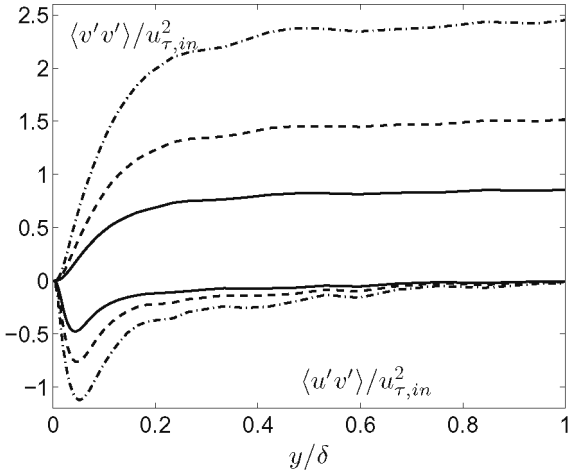

Figure 13. Shear stresses and wall-normal stresses. $x = 0.35\delta$. Investigation of sensitivity to different amplitude of inlet synthetic isotropic fluctuations. — : $u_{in,rms} = v_{in,rms} = w_{in,rms} = 0.75$; --- : $u_{in,rms} = v_{in,rms} = w_{in,rms} = 1.5$; ··· : $u_{in,rms} = v_{in,rms} = w_{in,rms} = 2.25$.

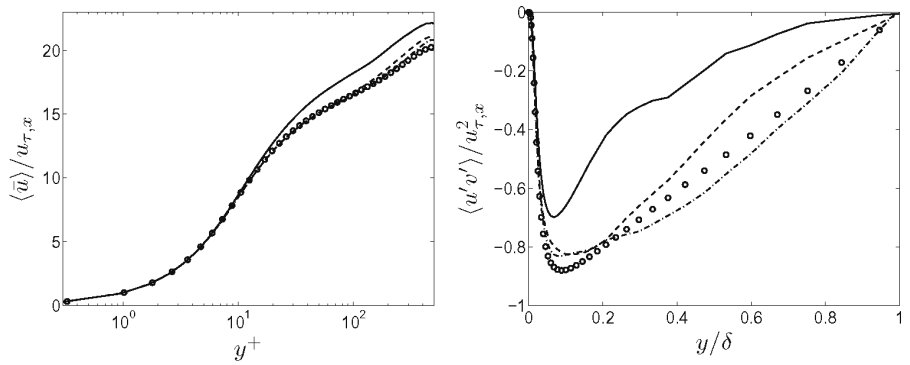

(a) $\langle \bar{u} \rangle$ profiles. (b) Resolved shear stresses.

Figure 14. Mean velocities and resolved shear stresses. Synthesized isotropic inlet fluctuating velocities. Synthetic fluctuations re-scaled to fit RMS profiles of DNS. Inlet time scale $\mathcal{T}_1$ and inlet length scale $\mathcal{L}_1$. o : inlet profiles; — : $x/\delta = 1$; --- : $x/\delta = 10$; -·- : $x/\delta = 24$.

In the results presented so far, constant RMS amplitudes of the isotropic fluctuations in the y direction have been used for $1/N_j < y/\delta < 2 - 1/N_j$. An alternative could be to re-scale the fluctuations so that the RMS profiles agree with DNS data of fully developed channel flow. The turbulent shear stress, $\langle (u'v')_{in} \rangle$, would still be zero, since the fluctuations are isotropic. It should be noted that it is not consistent to re-scale the fluctuations to yield nonhomogeneous normal stress profiles considering that the fluctuations were generated using Fourier series based on the assumption of homogeneous turbulence. Furthermore, when rescaling fluctuations, the two-point correlations in the y direction are modified and will be different from those shown in Fig. 8. Figure 14 gives velocity and shear stress profiles obtained with re-scaled synthetic inlet fluctuations. As can be seen, these fluctuations give much worse profiles than does constant RMS amplitude. The velocity profile at $x = \delta$ is over-predicted and the resolved shear stress is much too low. The friction velocity shown in Fig. 10 also shows that when re-scaled inlet fluctuations are used it takes a long distance before the friction velocity gets close to the target value.

It can be concluded from the DNS results presented above that inlet boundary conditions using synthetic, homogeneous, isotropic fluctuations give results almost as accurate as inlet conditions taken from a pre-cursor DNS. Furthermore, it was found that inlet fluctuations with a large time scale, large length scale and large amplitude are efficient in triggering the momentum equations to resolve turbulence. Having gathered some experience on how to prescribe inlet boundary conditions in DNS, we now turn our attention to the main object of the present study: inlet boundary conditions for hybrid LES-RANS.

6.2. Hybrid LES-RANS

A $64 \times 64 \times 32$ node mesh (x, streamwise; y, wall-normal; z, spanwise) was used. The size of the computational domain is $x_{\max} = 8\pi$, $y_{\max} = 2\delta = 2$ (geometric stretching of 17%) and $z_{\max} = 2\pi$. This gives a Δx^+ and Δz^+ of approximately 785 and 393, respectively and $y^+ < 1$ near the walls, expressed in inner scaling. In outer scaling $\delta/\Delta x \simeq 2.5$ and $\delta/\Delta z \simeq 5$. This mesh is very coarse and the resolution is realistic for industrial applications. The location of the matching plane is at $y = 0.075$ (lower wall) which corresponds to $y^+ = 150$ and 16 cells ($= j_{ml}$) in the URANS region at each wall, see Fig. 1. The time step was set to $\Delta t u_\tau/\delta = 4.91 \cdot 10^{-3}$ which gives a maximal CFL of approximately 0.6. The Reynolds number is $Re_\tau = u_\tau \delta/\nu = 2000$. Neumann boundary conditions are prescribed at the outlet.

Different time and length scales of the synthesized inlet turbulent fluctuations are evaluated, see Table 4. The base-line turbulent scales $\mathcal{T}_1$ and $\mathcal{L}_1$ are used in Fig. 15. The velocity profile is well predicted and resolved turbulence is created. Further downstream, the velocity in the center region increases slightly. The resolved turbulence is still too small close to the inlet ($x = \delta$). At this location the wall shear stress is over-predicted (see Fig. 16) because of the strong inlet fluctuations. The magnitudes of the resolved shear stresses increase further downstream and the friction velocity goes toward one. This scenario is similar to what was seen in the DNS simulations One difference, however, is that the

magnitude of the resolved shear stress is actually too large at $x = 10\delta$. The reason why the momentum equations are much more affected is because of the high Reynolds number and the very coarse grid resolution. With the prescribed inlet mean velocity profile, hybrid LES-RANS does not give a turbulent shear stress (sum of modelled and resolved) that is able to satisfy the time-averaged streamwise momentum equation. The result is that the flow is decelerated in the wall regions. The terms in the averaged streamwise momentum equations are presented in Fig. 17 (the wall normal advective term, $\langle\overline{v}\rangle\partial\langle\overline{u}\rangle/\partial y$, is not included because it is negligible). At $x = \delta$, the advection term, which in fully developed conditions should be zero, has the same magnitude as the turbulent diffusion. The forcing inlet fluctuations create a situation in which the averaged momentum equation is far from its fully developed flow condition. The advection term still plays an important role at $x = 10\delta$, especially in the center region. At the end of the domain ($x = 24\delta$), the advection term is rather small but still non-zero. Hence the flow is not fully developed. This can also be seen in Fig. 16, where the predicted friction velocity has not reached a constant value at the end of the domain.

Table 4. Presentation of test cases for hybrid LES-RANS simulations. $Re_\tau = 2000$. The baseline turbulent length scales and turbulent time scale are set to $\mathcal{L}_1 = 0.11 = L_t$ and $\mathcal{T}_1 = \mathcal{T} = 0.22$ (see Section 3), respectively. The baseline amplitude of the inlet fluctuations is $u_{in,rms} = v_{in,rms} = w_{in,rms} = 1.5$. The constants a and b from Eq. 5 are also given.

$\mathcal{L}$	$\mathcal{T}$	$u_{in,rms}$	a	b
$\mathcal{L}_1$	$\mathcal{T}_1/4$	1.5	0.90	0.43
$\mathcal{L}_1$	$\mathcal{T}_1$	1.5	0.974	0.223
$\mathcal{L}_1$	0	1.5	0	1
0	$\mathcal{T}_1$	1.5	0.974	0.223
$2\,\mathcal{L}_1$	$\mathcal{T}_1$	1.5	0.974	0.223
$\mathcal{L}_1$	$\mathcal{T}_1$	0.75	0.974	0.223
$\mathcal{L}_1$	$\mathcal{T}_1$	2.25	0.974	0.223

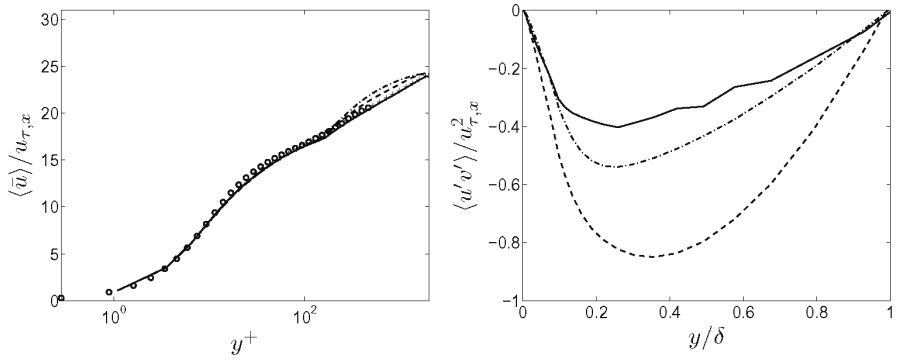

(a) $\langle \bar{u} \rangle$ profiles. +: $2.5 \ln(y^+) + 5.2$; ∘: fully developed 96^3 DNS.

(b) Resolved shear stresses.

Figure 15. Mean velocities and resolved shear stresses. Hybrid LES-RANS. Inlet time scale $\mathcal{T}_1$ and inlet length scale $\mathcal{L}_1$. — : $x/\delta = 1$; --- : $x/\delta = 10$; -·- : $x/\delta = 24$.

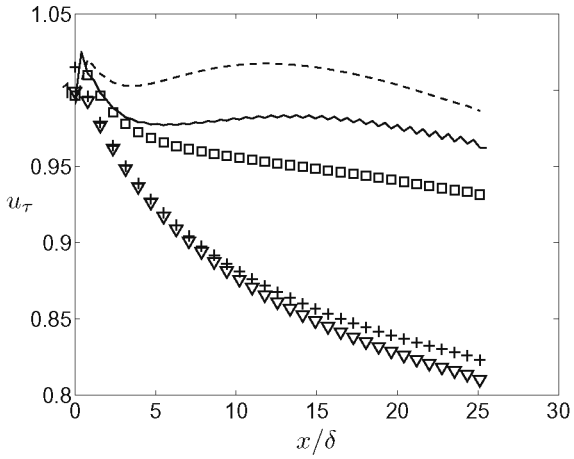

Figure 16. Friction velocity. Hybrid LES-RANS. — : $\mathcal{T}_1$ and $\mathcal{L}_1$; --- : $\mathcal{T}_1$ and $2\mathcal{L}_1$; + : $\mathcal{T}_1$ and $\mathcal{L} = 0$; ∇ : $\mathcal{T} = 0$ and $\mathcal{L}_1$; □ : $\mathcal{T}_1/4$ and $\mathcal{L}_1$.

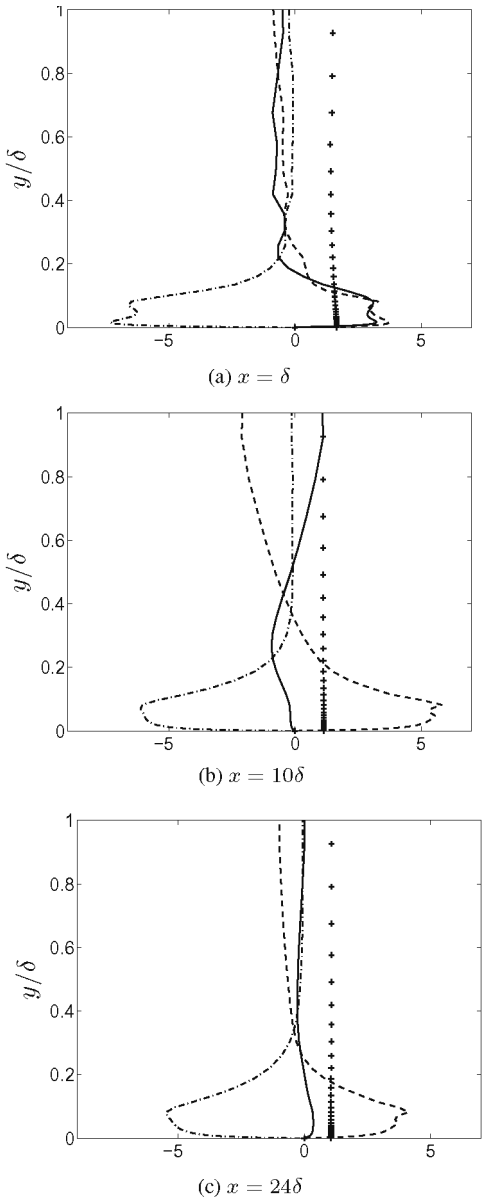

(a) $x = \delta$

(b) $x = 10\delta$

(c) $x = 24\delta$

Figure 17. Terms in the $\langle \overline{u} \rangle$ equation. Hybrid LES-RANS. Inlet time scale $\mathcal{T}_1$ and inlet length scale $\mathcal{L}_1$. — : $-\langle \overline{u} \rangle \partial \langle \overline{u} \rangle / \partial x$; --- : $-\partial \langle u'v' \rangle / \partial y$; -·- : $\partial / \partial y[(\nu + \nu_T) \partial \langle \overline{u} \rangle / \partial y]$; + : $-\partial \langle \overline{p} \rangle / \partial x$.

The friction velocity (solid line) in Fig. 16 exhibits typical odd-even oscillations. This is due to the coarse mesh and central differencing. These oscillations could easily be damped out using a wiggle detector [8] but, since they do not cause any problems, no damping was used. Oscillations are present in all cases, but all lines/markers except the solid line are plotted for every second x node to enhance visibility.

When the turbulence length scale of the inlet turbulence is increased from $\mathcal{L}_1$ to $2\mathcal{L}_1$, the predicted velocity profiles and resolved shear stresses are not to any great extent affected, see Fig. 18. It can be seen that the fluctuations with length scale $2\mathcal{L}_1$ are somewhat more efficient in creating resolved turbulence near the inlet than fluctuations with length scale $\mathcal{L}_1$. The result is a larger friction velocity, an even larger resolved shear stress at $x = 10\delta$ than in Fig. 15, and the advection term near the inlet is still larger.

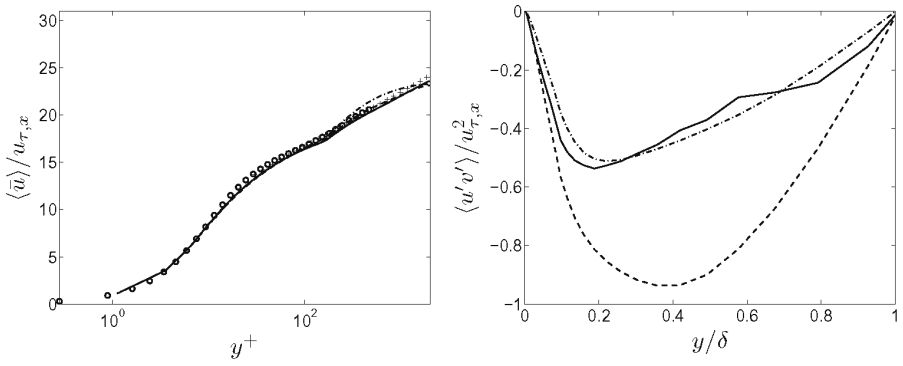

(a) $\langle\bar{u}\rangle$ profiles. +: $2.5\ln(y^+) + 5.2$; ∘: fully developed 96^3 DNS.

(b) Resolved shear stresses.

Figure 18. Mean velocities and resolved shear stresses. Hybrid LES-RANS. Inlet time scale $\mathcal{T}_1$ and inlet length scale $2\mathcal{L}_1$. — : $x/\delta = 1$; --- : $x/\delta = 10$; -·- : $x/\delta = 24$.

Next we test removing all turbulent spacial structures by setting the turbulent length scale to zero. Figure 19b shows that, compared to Fig. 15b, the generated resolved shear stresses are very small; at the outlet

the resolved shear stress has reached a value of only 0.2. Consequently the velocity in the center region in Fig. 19a is much too large due to the small resolved shear stress. The friction velocity is also much too small, see Fig. 16.

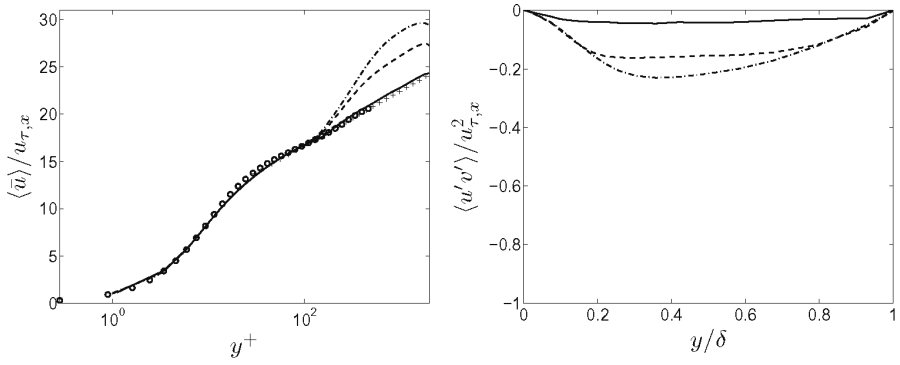

(a) $\langle \bar{u} \rangle$ profiles. +: $2.5 \ln(y^+) + 5.2$; ∘: fully developed 96^3 DNS.

(b) Resolved shear stresses.

Figure 19. Mean velocities and resolved shear stresses. Hybrid LES-RANS. Inlet time scale $\mathcal{T}_1$ and inlet length scale $\mathcal{L} = 0$. — : $x/\delta = 1$; --- : $x/\delta = 10$; -·- : $x/\delta = 24$.

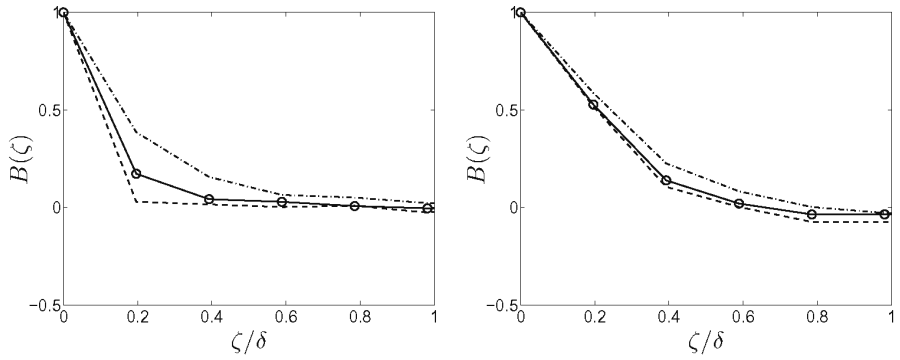

(a) $x = 0$.

(b) $x = 22.9\delta$.

Figure 20. Two-point correlation $B(\zeta) = 1/(z_{\max} w^2_{rms}) \int_0^{z_{\max}} w'(z)\, w'(z-\zeta) dz$. Hybrid LES-RANS. $y^+ \simeq 60$. Time scale $\mathcal{T}_1$. — : $\mathcal{L}_1$; --- : $\mathcal{L} = 0$; -·- : $2\mathcal{L}_1$. Markers illustrates the grid spacing.

Figure 20 shows the two-point correlations of the resolved turbulence at the inlet and at $x = 22.9\delta$ (both at $y^+ \simeq 60$) for the inlet turbulence scales $\mathcal{L} = 0$, $\mathcal{L}_1$ and $2\mathcal{L}_1$. At the inlet (Fig. 20a) the two-point correlation is of course zero for $\mathcal{L} = 0$. With $\mathcal{L}_1$ the correlation is approximately 0.2 at $\zeta = 0.2\delta = \Delta$ (the circles indicate the spanwise cell spacing), and the two-point correlation with $2\mathcal{L}_1$ is slightly more than twice as large at $\zeta = \Delta z$. However, far downstream (Fig. 20b), the difference in spanwise correlations between all three cases is not large. Thus, even for the case with no spanwise inlet correlation ($\mathcal{L} = 0$), some spanwise structures have been generated, although the velocity profile and resolved stress profile are very poorly predicted (Fig. 19). The fact that at $x = 22.9\delta$ some resolved turbulence has been created makes it likely that the velocity profiles and resolved stresses will be the same in all three cases for a very long channel. As mentioned in Section 1, the purpose of the inlet turbulent fluctuations is to *trigger* the equations into resolving turbulence. This triggering must be done at a scale that the equations understand. There is no point in using inlet turbulent fluctuations whose length scale is smaller than the grid scale. The turbulent length and time scales of the inlet fluctuations should not be as correct as possible, but they should be related to the grid and the discretization scheme.

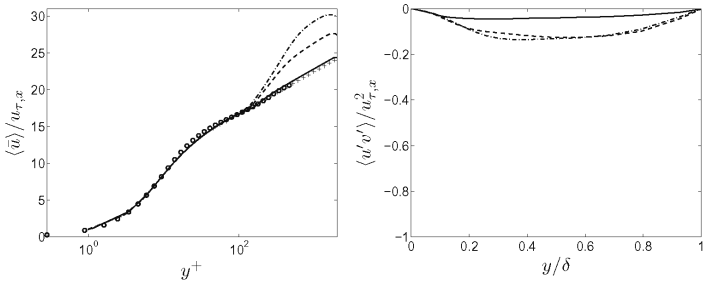

(a) $\langle \bar{u} \rangle$ profiles. $+$: $2.5\ln(y^+) + 5.2$; $\circ$: fully developed 96^3 DNS.

(b) Resolved shear stresses.

Figure 21. Mean velocities and resolved shear stresses. Hybrid LES-RANS. Inlet time scale $\mathcal{T} = 0$ and inlet length scale $\mathcal{L}_1$. — : $x/\delta = 1$; --- : $x/\delta = 10$; -·- : $x/\delta = 24$.

Figure 21 presents velocity and shear stress profiles where the turbulent time scale of the inlet fluctuations are set to zero ($a = 0$, $b = 1$ in Eq. 5, see Table 4). As can be seen, the equations have even greater problems coping with zero time scale than with zero length scale. The magnitude of the resolved shear stresses remains smaller than 0.15 throughout the channel.

Figure 16 shows the predicted friction velocity for all test cases. As has been observed in the velocity profiles, the poorest results are obtained for the cases for which the time scale, $\mathcal{T}$, or length scale, $\mathcal{L}$, are set to zero. With an inlet turbulent length scale of $\mathcal{L}_1$ the predicted friction velocity improves for the larger time scale. When the inlet length scale is increased to $2\mathcal{L}_1$ it is found that these fluctuations are too efficient in triggering the momentum equations.

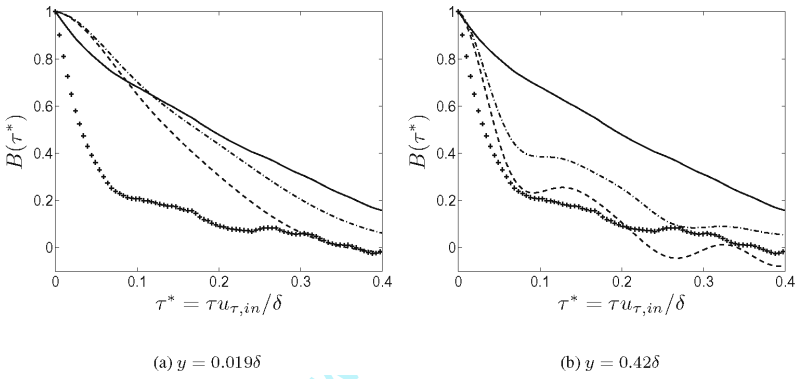

Figure 22. Autocorrelation $B(\tau)$. Hybrid LES-RANS. — : inlet, time scale $\mathcal{T}_1$; + : inlet, time scale $\mathcal{T}_1/4$; --- : $x = 22.9\delta$, inlet time scale $\mathcal{T}_1/4$; -·- : $x = 22.9\delta$, inlet time scale $\mathcal{T}_1$.

The autocorrelations are presented in Fig. 22. The autocorrelation at the inlet obviously increases when the prescribed time scale is increased from $\mathcal{T}_1/4$ to $\mathcal{T}_1$ via a and b, see Table 4. In the URANS region (Fig. 22a), the small inlet time scale $(\mathcal{T}_1/4)$ is increased far downstream because of the large turbulent viscosity (which yields large modelled dissipation) which dampens small time scales more than large time scales. In the case with the large inlet time scale $(\mathcal{T}_1)$ the predicted time

scale does not change much far downstream, because the prescribed time scale at the inlet fits the URANS region. In the LES region (Fig. 22b), the small inlet time scale is kept far downstream, whereas the large inlet time scale decreases far downstream. Again, this indicates that the small inlet time scale is close to the natural time scale of the LES region but that the large time scale is too large and in the latter case the LES region switches to its own time scale.

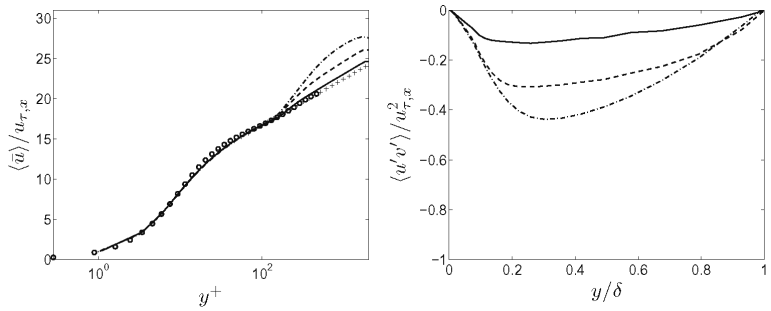

(a) $\langle\bar{u}\rangle$ profiles. +: $2.5\ln(y^+)+5.2$; ∘: fully developed 96^3 DNS.

(b) Resolved shear stresses.

Figure 23. Mean velocities and resolved shear stresses. Hybrid LES-RANS. Inlet time scale $\mathcal{T}_1$ and inlet length scale $\mathcal{L}_1$. $u_{in,rms} = v_{in,rms} = w_{in,rms} = 0.75$. — : $x/\delta = 1$; --- : $x/\delta = 10$; ··· : $x/\delta = 24$.

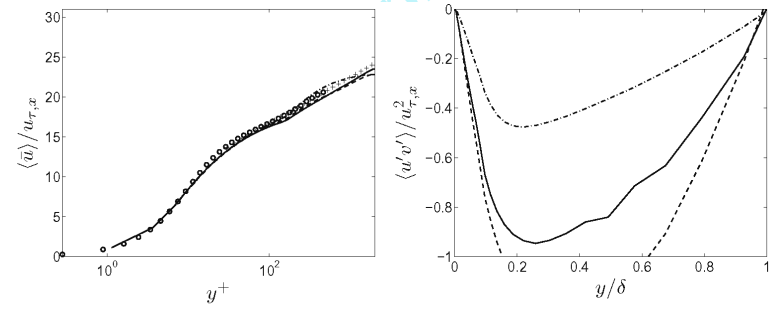

(a) $\langle\bar{u}\rangle$ profiles. +: $2.5\ln(y^+)+5.2$; ∘: fully developed 96^3 DNS.

(b) Resolved shear stresses.

Figure 24. Mean velocities and resolved shear stresses. Hybrid LES-RANS. Inlet time scale $\mathcal{T}_1$ and inlet length scale $\mathcal{L}_1$. $u_{in,rms} = v_{in,rms} = w_{in,rms} = 2.25$. — : $x/\delta = 1$; --- : $x/\delta = 10$; ··· : $x/\delta = 24$.

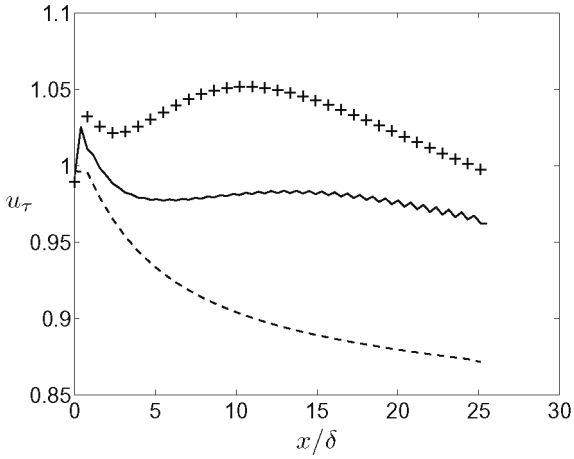

Figure 25. Friction velocity. Hybrid LES-RANS. Investigation of the influence of different amplitude of the inlet fluctuations. Inlet time scale $\mathcal{T}_1$ and inlet length scale $\mathcal{L}_1$. — : $u_{in,rms} = v_{in,rms} = w_{in,rms} = 1.5$ (baseline); --- : $u_{in,rms} = v_{in,rms} = w_{in,rms} = 0.75$; + : $u_{in,rms} = v_{in,rms} = w_{in,rms} = 2.25$.

We investigate next how a change in amplitude of the inlet fluctuations affects the flow. The baseline amplitude is $u_{in,rms} = v_{in,rms} = w_{in,rms} = 1.5$. It is reduced by 50% in Fig. 23 and it is increased by 50% in Fig. 24 compared to the baseline case in Fig. 15. As expected, a large amplitude is more efficient in triggering the equations than a small amplitude, and it is seen that the inlet fluctuations with the smallest amplitude (Fig. 23) generate much too small resolved shear stress at $x = \delta$. With the largest amplitude (Fig. 24), the equations are strongly disturbed by the inlet fluctuations, which lead to a large over-prediction in the shear stress at $x = 10\delta$. The three cases are compared in Fig. 25 where it can be seen that the smallest amplitude constitutes a poor inlet boundary condition. The largest amplitude gives a large over-prediction in friction velocity, but the flow has recovered far downstream from the strong disturbances generated by the inlet fluctuations and the flow at this location is actually well predicted.

6.3. Hybrid LES-RANS with forcing

A careful look at Fig. 16 reveals that the friction velocity decreases with x for all cases. The resolved turbulence – which was triggered at the inlet by the isotropic fluctuations – is slowly being dampened as x increases. Assume that we are using hybrid LES-RANS to simulate the flow in a diffuser or the flow over hill. Fluctuating inlet boundary conditions are prescribed. However from the decreasing friction velocities shown in Fig. 16, we should be concerned about what happens if the throat of the diffuser or the hill is located far from the inlet. If that is the case, the flow will be incorrect when it finally reaches the diffuser/hill because, as seen in Fig. 16, the friction velocity will be too small (or, more correctly, too low a ratio of the friction and centerline velocity). It is well known that standard LES-RANS gives too low a friction velocity for an infinitely long channel [2, 11, 22, 24, 26]. One way to overcome this deficiency in hybrid LES-RANS is to introduce forcing [2, 10, 11, 22, 24] – sometimes called back scatter or enrichment – in the near-wall (URANS) region or at the interface.

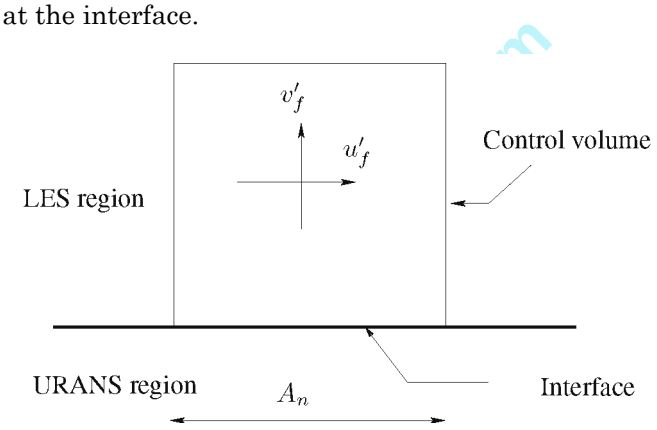

Figure 26. Added forcing fluctuations, u'_f, v'_f, w'_f, in a control volume $(j_{ml}+1)$ in the LES region adjacent to the interface.

The present work adopts the approach presented in [10]. The forcing is introduced as sources in the three momentum equations at the interface (see Figs. 1 and 26)

$$S_U = -\gamma\rho u'_f v'_f A_n = -\gamma\rho u'_f v'_f \Delta V/\Delta y$$

$$S_V = -\gamma\rho v_f' v_f' A_n = -\gamma\rho v_f' v_f' \Delta V/\Delta y$$

$$S_W = -\gamma\rho w_f' v_f' A_n = -\gamma\rho w_f' v_f' \Delta V/\Delta y, \tag{10}$$

where ΔV and Δy denote the cell volume and grid spacing in the y direction, respectively, and

$$\gamma = k_T(x,\, y_{ml},\, z)/k_f, \quad k_f = \frac{1}{2}(u_{f,rms}^2 + v_{f,rms}^2 + w_{f,rms}^2) \tag{11}$$

u_f', v_f', w_f' denote synthetic isotropic fluctuations generated in the same way as the inlet fluctuations. See [10] for more details.

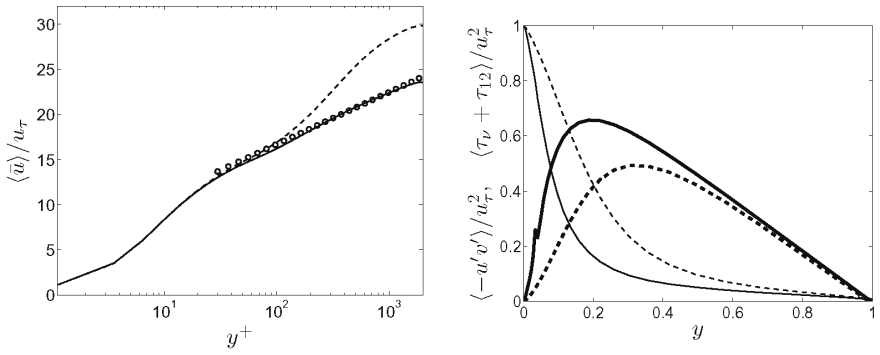

(a) $\langle\bar{u}\rangle$ profiles. ∘: $2.5\ln(y^+) + 5.2$

(b) Shear stresses. τ_ν denotes viscous stress. Thick lines: resolved; thin lines: modelled.

Figure 27. Mean velocities and shear stresses. Hybrid LES-RANS. Periodic streamwise boundary conditions. Solid lines: forcing with isotropic fluctuations; dashed lines: no forcing.

In Fig. 27a the velocity profiles are presented using forcing and no forcing. As can be seen, the agreement with the law of the wall using hybrid LES-RANS with forcing is excellent. Without forcing, agreement is less good.

The resolved and modelled shear stresses are shown in Fig. 27b for the two hybrid models. The resolved stress using forcing is larger than without forcing. The reason is that the forcing fluctuations trigger the momentum equations to resolve turbulence. Since the total shear stress must follow $1 - y$, the modelled shear stress with forcing is smaller than without forcing.

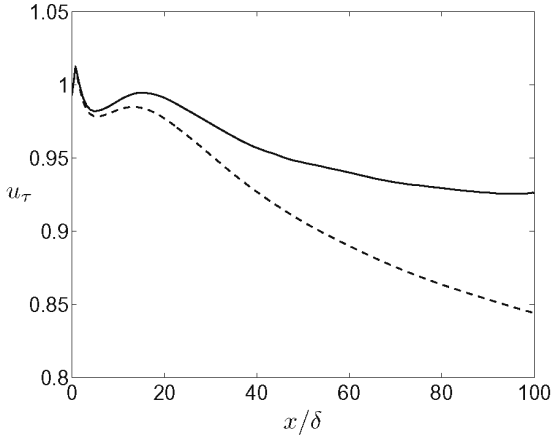

Figure 28. Friction velocity. Hybrid LES-RANS. $\mathcal{T}_1$ and $\mathcal{L}_1$. — : forcing; --- : no forcing.

In Fig. 28 hybrid LES-RANS with and without forcing is used for a long channel ($256 \times 64 \times 32$ cells, $x_{\max} = 32\pi\delta$). Without forcing, the friction velocity is still decreasing at the outlet whereas with forcing the friction velocity decreases down to $u_\tau \simeq 0.93$. Hence, with forcing, the inlet can be located very far downstream without any large adverse effect.

Considering the accurate velocity profile predicted using forcing for an infinitely long channel (i.e., with streamwise periodic boundary conditions), see Fig. 27a, it may seem somewhat unexpected that the friction velocity predicted using forcing (Fig. 28) does not approach the target value $u_\tau = 1$. The reason is that in the buffer region the prescribed inlet mean velocity profile (see Eq. 6) does not entirely agree with the mean profile shown in Fig. 27a.

7. Conclusions

In the present paper isotropic synthetic fluctuations have been used to prescribe realistic turbulent inlet boundary conditions. For DNS simulations this approach was compared with inlet conditions taken from a pre-cursor DNS. The two methods were found to be comparable (the pre-cursor DNS slightly better) and both methods were found to give a wall friction velocity, u_τ, within 1% of the target value at less than five

half-channel widths downstream of the inlet. Quite reasonably resolved shear stress profiles are obtained with synthesized fluctuations as early as one half-channel width downstream of the inlet.

The influence of different turbulent inlet length scales, time scales and amplitudes of the synthetic fluctuations have been investigated. It was found that inlet fluctuations with a large time scale, large length scale and large amplitude are efficient in triggering the momentum equations to resolve turbulence. A large length scale may lead to too violent forcing of the equations and lead to over-predicted resolved stresses, at least in connection with DNS.

It has been shown that it is necessary to prescribe both a realistic length scale and time scale of the inlet fluctuations. If zero length or time scale is used, then the resulting resolved fluctuations are much too small. It is also important that the amplitude of the fluctuations is sufficiently large. A value of $u_{in,rms}/u_\tau = 0.75$ is too small, whereas $u_{in,rms}/u_\tau = 1.5$ is sufficient.

In all simulations carried out in the present work except one, the RMS of the synthesized fluctuations was constant across the inlet (except for $y < \Delta\eta$, lower wall, and $y > 2\delta - \Delta\eta$, upper wall). In one simulation the fluctuations were re-scaled so that the normal stresses of the synthesized fluctuations were equal to those of a DNS at a lower Reynolds number. This re-scaling modifies the two-point correlations in the wall-normal direction and hence also the prescribed turbulence length scale. It was found that this approach gave considerably poorer results than when no re-scaling was used.

Standard hybrid LES-RANS yields too small wall shear stress (or, equivalently, too large centerline velocity) in infinitely long channels. One way to reduce this deficiency is to introduce forcing at the interface or in the interface region. It is argued that fluctuating inlet boundary conditions should be viewed as *forcing* conditions with the object of triggering the equations to resolve turbulence. Hence, it is not important that the length scale and time scale are physically correct. They should be chosen on the basis of their being efficient in triggering the equations, and they should be related to the grid, the time step, the discretization

scheme, the turbulence model and the location of the inlet. If the inlet is located, for example, far upstream of a slanted surface along which separation is expected to take place, it may occur that the resolved turbulence triggered at the inlet is dissipated before the flow reaches the slanted surface. In this case additional forcing is needed at the interface between the LES region and the URANS region to keep the resolved turbulence alive. The flow in a long channel was computed to exemplify this problem.

Acknowledgement

This work was financed by the DESider project (Detached Eddy Simulation for Industrial Aerodynamics) which is a collaboration between Alenia, ANSYS-AEA, Chalmers University, CNRS-Lille, Dassault, DLR, EADS Military Aircraft, EUROCOPTER Germany, EDF, FOI-FFA, IMFT, Imperial College London, NLR, NTS, NUMECA, ONERA, TU Berlin, and UMIST. The project is funded by the European Community represented by the CEC, Research Directorate-General, in the 6th Framework Programme, under Contract No. AST3-CT-2003-502842.

References

[1] C. Bailly and D. Juvé, A stochastic approach to compute subsonic noise using linearized Euler's equations, AIAA paper 99-1872, 1999.

[2] P. Batten, U. Goldberg and S. Chakravarthy, Interfacing statistical turbulence closures with large-eddy simulation, AIAA Journal 42(3) (2004), 485-492.

[3] W. Bechara, C. Bailly and P. Lafon, Stochastic approach to noise modeling for free turbulent flows, AIAA Journal 32(3) (1994), 455-463.

[4] M. Billson, L.-E. Eriksson and L. Davidson, Jet noise prediction using stochastic turbulence modeling, AIAA paper 2003-3282, 9th AIAA/CEAS Aeroacoustics Conference, 2003.

[5] M. Billson, L.-E. Eriksson and L. Davidson, Modeling of synthetic anisotropic turbulence and its sound emission, The 10th AIAA/CEAS Aeroacoustics Conference, AIAA 2004-2857, Manchester, United Kingdom, 2004.

[6] M. Billson, Computational techniques for turbulence generated noise, Ph.D. Thesis, Dept. of Thermo and Fluid Dynamics, Chalmers University of Technology, Göteborg, Sweden, 2004.

[7] S. Dahlström and L. Davidson, Hybrid RANS-LES with additional conditions at the matching region, Turbulence Heat and Mass Transfer 4, K. Hanjalić, Y. Nagano, and M. Tummers, eds., Begell House, Inc., New York, Wallingford (UK), 2003, pp. 689-696.

[8] S. Dahlström and L. Davidson, Large eddy simulation applied to a high-Reynolds flow around an airfoil close to stall, AIAA paper 2003-0776, 2003.

[9] L. Davidson and S.-H. Peng, Hybrid LES-RANS: A one-equation SGS model combined with a $k-\omega$ model for predicting recirculating flows, International Journal for Numerical Methods in Fluids 43 (2003), 1003-1018.

[10] L. Davidson and M. Billson, Hybrid LES/RANS using synthesized turbulence for forcing at the interface, International Journal of Heat and Fluid Flow 27(6) (2006), 1028-1042.

[11] L. Davidson and S. Dahlström, Hybrid LES-RANS: An approach to make LES applicable at high Reynolds number, International Journal of Computational Fluid Dynamics 19(6) (2005), 415-427.

[12] P. Emvin, The full multigrid method applied to turbulent flow in ventilated enclosures using structured and unstructured grids, Ph.D. Thesis, Dept. of Thermo and Fluid Dynamics, Chalmers University of Technology, Göteborg, 1997.

[13] F. Hamba, A hybrid RANS/LES simulation of turbulent channel flow, Theoretical and Computational Fluid Dynamics 16 (2003), 387-403.

[14] N. Jarrin, S. Benhamadouche and D. Laurence, Inlet conditions for large-eddy simulation using a new vortex method, The Fourth International Symp. on Turbulence and Shear Flow Phenomena, J. Humphrey, J. Eaton, R. Friedrich, N. Kasagi, M. Leschziner, and T. Gatski, eds., Williamsburg, Virginia, 2005.

[15] M. Karweit, P. Blanc-Benon, D. Juvé and G. Comte-Bellot, Simulation of the propagation of an acoustic wave through a turbulent velocity field: A study of phase variance, J. Acoust. Soc. Am. 89(1) (1991), 52-62.

[16] M. Klein, A. Sadiki and J. Janicka, A digital filter based generation of inflow data for spatially developing direct numerical or large Eddy simulations, J. Computational Physics 186(2) (2003), 652-665.

[17] R. Kraichnan, Diffusion by a random velocity field, Physics of Fluids 13 (1970), 22-31.

[18] J. Larsson, F. Lien and E. Yee, Large eddy simulation of high Reynolds number channel flow on coarse grids, 13th Annual Conference of the Computational Fluid Dynamics Society of Canada, 2005, pp. 61-68.

[19] H. Le and P. Moin, Direct numerical simulation of turbulent flow over a backward facing step, Report no. TF-58, Stanford University, Dept. Mech. Eng., 1994.

[20] H. Le, P. Moin and J. Kim, Direct numerical simulation of turbulent flow over a backward-facing step, Journal of Fluid Mechanics 330 (1997), 349-374.

[21] S. Lee, S. Lele and P. Moin, Simulation of spatially evolving turbulence and the application of Taylor's hypothesis in compressible flow, Physics of Fluids A 4 (1992), 1521-1530.

[22] U. Piomelli, E. Balaras, H. Pasinato, K. Squire and P. Spalart, The inner-outer layer interface in large-eddy simulations with wall-layer models, International Journal of Heat and Fluid Flow 24 (2003), 538-550.

[23] A. Smirnov, S. Shi and I. Celik, Random flow generation technique for large eddy simulations and particle-dynamics modeling, Journal of Fluids Engineering 123(2) (2001), 359-371.

[24] L. Temmerman, M. Hadžiadbic, M. Leschziner and K. Hanjalić, A hybrid two-layer URANS-LES approach for large eddy simulation at high Reynolds numbers, International Journal of Heat and Fluid Flow 26 (2005), 173-190.

[25] P. Tucker, Differential equation based length scales to improve DES and RANS simulations, AIAA paper 2003-3968, 16th AIAA CFD Conference, 2003.

[26] P. Tucker and L. Davidson, Zonal k-l based large eddy simulation, Computers & Fluids 33(2) (2004), 267-287.

[27] J. Welty, C. E. Wicks and R. Wilson, Fundamentals of Momentum, Heat, and Mass Transfer, 3rd ed., John Wiley & Sons, New York, 1984.

[28] X. Xiao, J. Edwards and H. Hassan, Inflow boundary conditions for LES/RANS simulations with applications to shock wave boundary layer interactions, AIAA paper 2003-0079, Reno, NV, 2003.

■